

# Turbulence destroys thermal lobes around Mars-sized planetary embryos

R. O. Chametla<sup>1</sup>, A. Moranchel-Basurto<sup>1</sup>, and F. J. Sánchez-Salcedo<sup>2</sup>

<sup>1</sup> Charles University, Faculty of Mathematics and Physics, Astronomical Institute, V Holešovičkách 747/2, 180 00, Prague 8, Czech Republic

e-mail: raul@sirrah.troja.mff.cuni.cz

<sup>2</sup> Instituto de Astronomía, Universidad Nacional Autónoma de México, Apt. Postal 70-264, C.P. 04510, Mexico City, Mexico

Received XXX; accepted YYY

## ABSTRACT

**Context.** The release of heat by a planetary embryo modifies the local density perturbations, forming thermal lobes in its vicinity, and thereby altering the torque exerted by the disk on the embryo. In laminar disks, these thermal torques can dominate the disk-embryo interaction, rendering the classical Lindblad and corotation torques largely subdominant.

**Aims.** The aim of this work is to investigate how turbulence driven by the magnetorotational instability affects the thermal lobes formed around a planetary embryo, and to analyze the resulting torque acting on the embryo.

**Methods.** We evaluate the thermal torques exerted on a planetary embryo of mass  $M_p = 0.33M_{\oplus}$  (with  $M_{\oplus}$  is the mass of Mars) and on a planetary core with mass  $M_p = 1M_{\oplus}$ , each embedded in a turbulent gaseous protoplanetary disk, by means of high-resolution three-dimensional magnetohydrodynamics simulations that include thermal diffusion and an initially toroidal magnetic field. The magnetic field strength is characterized by the plasma  $\beta$  plasma parameter with  $\beta \in \{50, 1000\}$ . We consider two values for the luminosity of the planetary embryo:  $L = 0$  (cold thermal lobes) and  $L = L_c$  (hot thermal lobes), where  $L_c$  represents the critical luminosity. For the  $0.33M_{\oplus}$  embryo,  $L_c = 7.8 \times 10^{25} \text{ ergs s}^{-1}$  when it orbits a Sun-like star at a distance  $r_p = 5.2 \text{ au}$ .

**Results.** We find that, even in the presence of a weak magnetic field and irrespective of the luminosity, for both planetary masses, the development of turbulence in the disk (which takes between 1.5 to 3 orbital periods) completely disrupts the thermal lobes. As a result, the torque acting on both the planetary embryo and the Earth-mass core displays a strongly oscillatory behavior. This suggests that planets with masses in the range  $0.03M_{\oplus} \lesssim M_p \lesssim 1M_{\oplus}$  experience stochastic migration, as expected in turbulent disks.

**Conclusions.** Thermal torques become inefficient in turbulent regions of protoplanetary disks, such as outside the dead zone, in both the inner and outer disk regions where the magnetorotational instability operates.

**Key words.** protoplanetary disks – planet-disk interaction – magnetohydrodynamics

## 1. Introduction

In recent years, thermal torques on low-mass planets and planetary embryos embedded in regions of the gaseous protoplanetary disks where the flux is laminar (Lega et al. 2014; Masset 2017; Benítez-Llambay et al. 2015; Chametla & Masset 2021) have emerged as a possible solution to the problem of fast inward migration (see Paardekooper et al. 2023, for a review). Thermal torques on a planet are due to the asymmetric gas density structures formed in the vicinity of the planet, which result from thermal diffusion in the disk. When a planet accretes pebbles, it releases heat into the environment, producing the formation of low-density, asymmetric hot lobes in the disk. These lobes, in turn, produce a torque on the planet (the heating torque; Masset 2017). If the planet does not accrete pebbles, thermal diffusion produces the formation of high-density cold lobes in the coorbital region of the planet (the cold thermal torque; Lega et al. 2014; Masset 2017). Both heating and cold thermal torques can exceed the Lindblad and corotation torques by up to an order of magnitude, such that the Lindblad and corotation torques become negligible. Heating thermal torques can slow down, or even reverse, the inward migration of growing low-mass planets (Benítez-Llambay et al. 2015).

Using global disc models, Guilera et al. (2019) showed that thermal torques can modify both migration maps and planet for-

mation tracks, i.e. the evolution of the planetary mass as a function of semi-major axis (but see also Baumann & Bitsch 2020). In a more comprehensive framework of mass growth by pebble accretion, Guilera et al. (2021) found that thermal torques play a significant role in shaping planet formation tracks in low-viscosity disks, particularly when the disks are both massive and metal-rich. Under these conditions, planets forming beyond the ice line may undergo substantial outward migration.

Thermal forces can also excite eccentricity and inclination. In a model that additionally follows the evolution of eccentricity and inclination for a population of pebble-accreting embryos, Cornejo et al. (2023) reported that the inclusion of thermal torques leads to a markedly different dependence of the final embryo mass spectrum on disk metallicity. The excitation of eccentricity by thermal torques may also have important implications for the trapping and formation of planets in pressure bumps (Chrenko & Chametla 2023; Pierens & Raymond 2024; Velasco-Romero et al. 2024a).

All studies of thermal torques to date have been conducted under the assumption of an unmagnetized, laminar disk. However, there exist regions of protoplanetary disks in which turbulence is expected to dominate the transport of angular momentum. In such turbulent environments, it has been shown that the migration of planetary embryos can become stochastic (Nelson

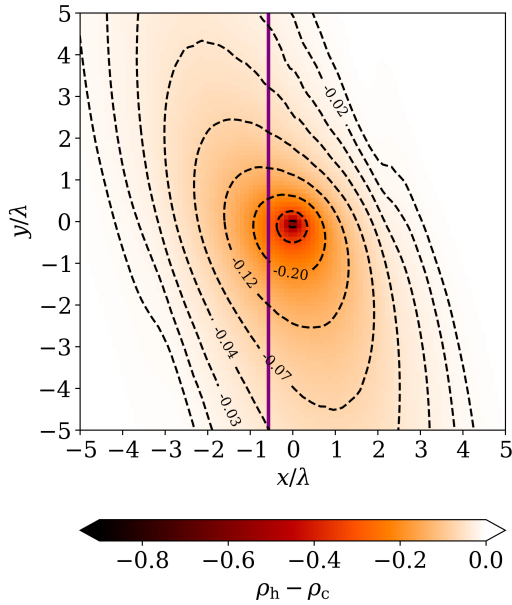


Fig. 1: Perturbation of density arising from heat release obtained by subtracting a hot run ( $L = L_c$ ) and a cold run ( $L = 0$ ) for the case  $\beta = 50$  at  $t = 1$  orbit. The perturbation is integrated over colatitude and normalized to  $\gamma(\gamma - 1)L/\chi c_s^2$ . The purple solid line indicates the corotation radius.

& Papaloizou 2004; Nelson 2005). This occurs, for instance, outside the dead zone, where strong magnetic coupling enables turbulence driven by the magnetorotational instability (MRI; Balbus & Hawley 1991). In addition, hydrodynamical instabilities may also lead to turbulence even within the dead zone (see Lyra & Umurhan 2019). In this work, we assess whether thermal torques remain effective in driving the migration of low-mass planets or planetary embryos in turbulent regions of the disk. To address this, we conduct high-resolution MHD simulations of a planetary embryo embedded in a thermally diffusive, stratified protoplanetary disk threaded by a toroidal magnetic field.

The paper is laid out as follows. Section 2 describes the MHD equations, the numerical setup, and the code used in this work. In Section 3 we present our results. A brief discussion of possible improvements in more complex models is presented in Section 4. Finally, concluding remarks can be found in Section 5.

## 2. Physical and numerical setup

We consider a 3D magnetized, inviscid gas disk whose dynamical evolution is described by the MHD equations:

$$\partial_t \rho + \nabla \cdot (\rho \mathbf{v}) = 0, \quad (1)$$

$$\partial_t (\rho \mathbf{v}) + \nabla \cdot (\rho \mathbf{v} \otimes \mathbf{v} + p \mathbf{I}) = -\rho \nabla \Phi + \mathbf{J} \times \mathbf{B}, \quad (2)$$

$$\partial_t e + \nabla \cdot (e \mathbf{v}) = -p \nabla \cdot \mathbf{v} - \nabla \cdot \mathbf{F}_H + S_p, \quad (3)$$

$$\frac{\partial \mathbf{B}}{\partial t} = \nabla \times (\mathbf{v} \times \mathbf{B}), \quad (4)$$

where  $\rho$  and  $\mathbf{v}$  denote the gas density and velocity, respectively, and  $\mathbf{J}$  and  $\mathbf{B}$  the current density and magnetic field.  $\mathbf{I}$  denotes the unit tensor and  $\Phi$  the gravitational potential. For the gravitational potential of the planetary embryo we adopt a softening

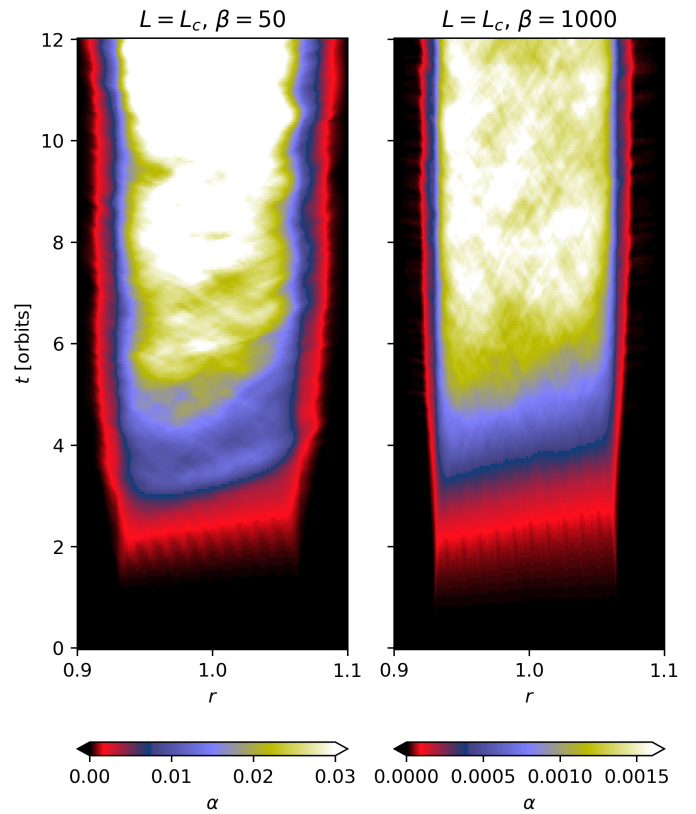


Fig. 2: Temporal evolution of  $\alpha$ , defined by Eq. (15), for the runs with  $L = L_c$  and  $\beta = 50$  (left panel) and  $\beta = 1000$  (right panel).

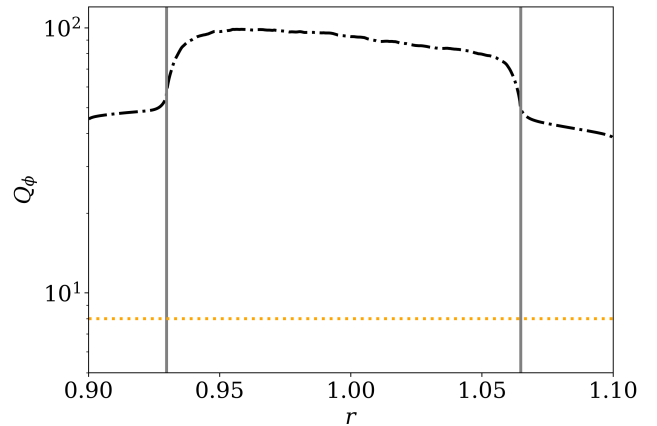


Fig. 3: Quality factor averaged over space and time. The orange dotted line shows the eight-cell limit. The vertical gray lines delineate the buffer zones.

length comparable to our mesh resolution. For the pressure  $p$ , we consider the equation of state

$$p = (\gamma - 1)e, \quad (5)$$

where  $e$  is the internal energy density and  $\gamma = 7/5$  the gas adiabatic index.

In Eq. (3),  $S_p$  is a source term arising from the energy release of the planetary embryo defined as

$$S_p = L\delta(\mathbf{r} - \mathbf{r}_p) \quad (6)$$

with  $L$  and  $\mathbf{r}_p$  the luminosity and the location of the planet, respectively, and  $\delta$  the Dirac's delta function. While  $\mathbf{F}_H$  is the heat flux, given by

$$\mathbf{F}_H = -\chi\rho\nabla\left(\frac{e}{\rho}\right), \quad (7)$$

where  $\chi$  is the thermal diffusivity. This advection-diffusion approximation has been commonly adopted in previous studies (e.g., Masset 2017; Velasco Romero & Masset 2020; Chametla & Masset 2021; Chametla et al. 2025). Other authors instead employ the flux-limited diffusion scheme within a two-temperature framework (Benítez-Llambay et al. 2015). In the regime considered here, however, both approaches describe radiative transport in the diffusion limit, and therefore we do not expect significant differences in the resulting thermal torques.

### 2.1. Set-up

We largely follow the setup of Chametla & Masset (2021). Only a brief summary is given here. We consider a 3D patch of a non-self-gravitating disk. The simulations are performed in a frame co-rotating with the planetary embryo, using a polar spherical grid centered on the star. The numerical domain extends for  $0.9r_p$  to  $1.1r_p$  in the radial direction, from  $-\pi/18$  to  $\pi/18$  in the azimuthal direction and between  $\pi/2 - h_p$  and  $\pi/2 + h_p$  in colatitude (here  $h_p = 0.05$  is the aspect ratio at the position of the planetary embryo). The simulations employ  $(N_r, N_\theta, N_\phi) = (880, 128, 1536)$  grid zones, corresponding to cell sizes of  $(2.3 \times 10^{-4}r_p, 7.8 \times 10^{-4}r_p, 2.3 \times 10^{-4}r_p)$ .

Initially, the surface density and temperature follow constant radial profiles, i.e.  $\Sigma \propto r^{-\sigma}$  and  $T \propto r^{-\zeta}$ , with  $\sigma = \zeta = 0$ . The disk is initially threaded by a toroidal magnetic field given by

$$B_\phi = H\Omega\sqrt{\frac{8\pi\rho}{\beta}}, \quad (8)$$

whose strength is parameterized by the plasma- $\beta$  parameter, with  $\beta = 50$  and  $1000$ . Here,  $H$  denotes the pressure scale length.

We consider a planetary embryo of mass  $M_p$ , with a luminosity of  $L \in \{0, L_c\}$ , where  $L_c$  is the critical luminosity

$$L_c = \frac{4\pi GM_p\chi\rho_0}{\gamma}, \quad (9)$$

with  $\rho_0 = \Sigma_0/(\sqrt{2\pi}H)$  the unperturbed midplane density at  $r = r_p$  (Masset 2017). For  $L > 0.94L_c$ , heat release dominates over thermal diffusion and the total thermal torque is positive, whereas for  $L < 0.94L_c$  diffusion dominates and the total thermal torque is negative. At  $L = 0.94L_c$ , the thermal contribution vanishes (see Fig. 6 Chametla & Masset 2021). We set thermal diffusivity to  $\chi = 10^{-5}r_p^2\Omega_p$ .

Since planetary embryos are the seeds from which larger planets grow, a natural first step is to investigate whether the thermal torques that govern their migration in laminar disks (where they can slow down or even reverse migration and thereby favor their growth) remain effective in a turbulent medium. Therefore, unless otherwise stated, we adopt  $M_p = 0.33M_\oplus$ , with  $M_\oplus$  the mass of Mars. In physical units, further adopting  $r_p = 5.2$  au and  $\Sigma_0 = 208$  g cm $^{-2}$  yields  $\chi = 1.1 \times 10^{20}$  cm $^2$  s $^{-1}$  and  $L_c = 7.8 \times 10^{25}$  erg s $^{-1}$ . The value of  $\chi$  appears reasonable at this distance from the central star. In principle, the results of our simulations can be rescaled to a different orbital radius  $r_p$ . In that case, the thermal diffusivity scales as  $\chi = 1.1 \times 10^{20}(r/5.2 \text{ au})^{1/2}$  cm $^2$  s $^{-1}$ .

At large radii, however, this simple scaling is expected to deviate from the true value because the radial dependencies of the opacity (Bell & Lin 1994), density, and temperature are unlikely to conspire to produce such a scaling of the diffusivity. Therefore, caution must be exercised when rescaling the simulation results to other orbital distances.

### 2.2. Code and boundary conditions

To solve the continuity, momentum and energy equations for the gas, we use the hydrodynamic public FARGO3D multifluids code (Benítez-Llambay et al. 2019), which is an extended version of the original FARGO3D code (Benítez-Llambay & Masset 2016), with orbital advection enabled (Masset 2000).

A thermal diffusion module was included in the code FARGO3D<sup>1</sup> multifluids. This module was already tested and used in Chametla & Masset (2021) for the numerical study of thermal torques in a gaseous disk without magnetic fields. Using an operator-splitting scheme, the thermal diffusion term in the energy equation was evolved separately. Specifically, during the diffusion update the internal energy satisfies

$$\partial_t e = -\nabla \cdot \mathbf{F}_H. \quad (10)$$

The source energy term  $S_p$ , representing the heat release of the planetary embryo, was implemented by increasing the internal energy density over eight adjacent grid cells (Benítez-Llambay et al. 2015; Chametla & Masset 2021; Velasco-Romero et al. 2024b)

$$\Delta e_{i,j,k} = L \left(1 - \frac{\phi_{i,j,k}^p}{\Delta\phi}\right) \left(1 - \frac{r_{i,j,k}^p}{\Delta r}\right) \left(1 - \frac{\theta_{i,j,k}^p}{\Delta\theta}\right) \frac{\Delta t}{V_{i,j,k}}, \quad (11)$$

where  $L$  is the luminosity,  $V_{i,j,k}$  the volume of the cell  $(i, j, k)$ ,  $\phi_{i,j,k}^p = |\phi_p - \phi_{i,j,k}|$ ,  $r_{i,j,k}^p = |r_p - r_{i,j,k}|$ ,  $\theta_{i,j,k}^p = |\theta_p - \theta_{i,j,k}|$  and  $\Delta t$  is the difference between each timestep.

The boundary conditions follow those implemented for the gas density and velocity components in Chametla & Masset (2021). We include magnetic resistivity buffer zones in the radial and vertical directions of the disk, covering the same computational domain as the hydrodynamical damping zones.

### 2.3. Parameters and relevant scales within thermal torques theory

Linear theory predicts that the size of the thermal disturbance is given by

$$\lambda_c = \sqrt{\frac{\chi}{(3/2)\Omega_p\gamma}} \quad (12)$$

(Masset 2017). The level of asymmetry of the thermal perturbations is determined by the planetary embryo's corotation offset, which is given by

$$x_p = \eta h_p^2 r_p, \quad (13)$$

where  $\eta$  is a function of the power-law exponents of the surface density and temperature, given by

$$\eta = \frac{\sigma}{3} + \frac{\zeta + 3}{6}. \quad (14)$$

In our case, for  $\sigma = \zeta = 0$ , the parameter  $\eta$  reduces to  $1/2$ .

<sup>1</sup> The version of this code without the thermal diffusion module is available in <https://fargo3d.github.io/documentation/>

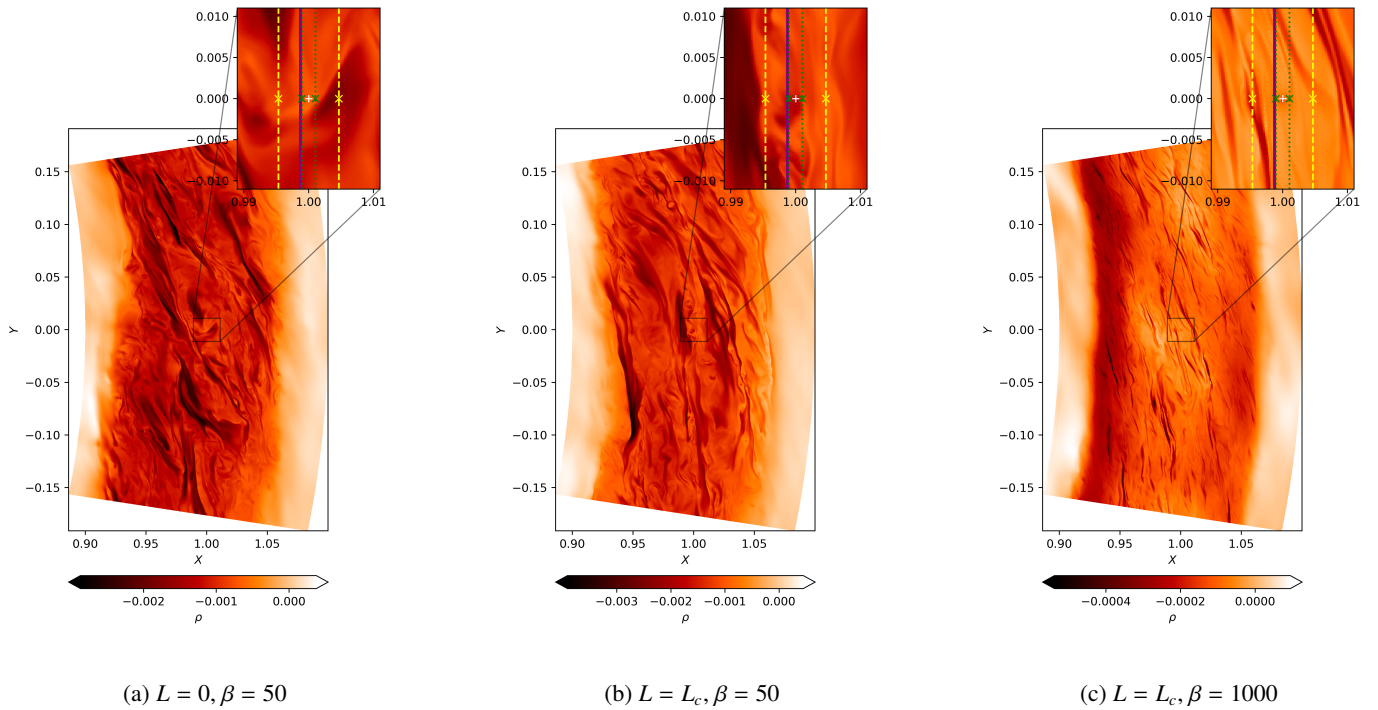


Fig. 4: Gas density (logarithmic scale) at the midplane at  $t = 11$  orbits. The zoomed regions correspond to an area similar to that shown in Fig. 1 around the planetary embryo. In these regions, no low-density structures resembling hot lobes are observed. The purple solid lines indicate the corotation radii. The yellow dashed and green dotted lines mark the locations of the magnetic resonances for  $\beta = 50$  and  $\beta = 1000$ , respectively. The white plus symbol denotes the position of the planetary embryo.

### 3. Results

#### 3.1. The turbulent disk

For the adopted disk parameters, Eqs. (12) and (13) yield  $x_p = 1.25 \times 10^{-3} r_p$ ,  $\lambda_c = 2.2 \times 10^{-3} r_p$ , and  $H = 0.05 r_p$ . The ordering  $x_p \leq \lambda_c \ll H$  implies that the density perturbation induced by the planetary embryo's luminosity should be observable, at least in the absence of turbulence or prior to its full development, which occurs after approximately three orbital periods. To verify this expectation, Fig. 1 presents the density perturbation for  $L = L_c$  and  $\beta = 50$  after  $t = 1$  orbit, i.e. before turbulence has had time to grow. At this stage, the hot lobes are already fully formed and exhibit a pronounced asymmetry with respect to the planetary embryo's position. This behavior is characteristic of the evolution of hot lobes in a turbulence-free gas disk (Chametla & Masset 2021).

The onset of turbulence is illustrated in Fig. 2, which shows the temporal evolution of the stress-to-pressure ratio  $\alpha$ , a measure of the strength of the turbulence in the disk, computed as

$$\alpha(r, t) = \frac{\int (\rho \delta v_r \delta v_\phi - B_r B_\phi / 4\pi) r^2 \sin \theta d\theta d\phi}{\int p r^2 \sin \theta d\theta d\phi}, \quad (15)$$

for models with  $L = L_c$  and for the two values  $\beta = 50$  and  $\beta = 1000$ . The development of MRI-driven turbulence begins at  $t \sim 1.8$  orbits, and by  $t = 3$  orbits  $\alpha$  already exceeds  $10^{-4}$ . Note that when turbulence is fully developed,  $\alpha$  reaches the values of  $10^{-3}$  and  $10^{-2}$ , when  $\beta = 1000$  and  $\beta = 50$ , respectively.

To ensure that the MRI is well resolved in our models, we compute the quality factor  $Q_\phi$  (Sorathia et al. 2012; Flock et al.

2017)

$$Q_\phi = 2\pi \sqrt{\frac{16}{15}} \frac{|B_\phi|}{\sqrt{4\pi\rho}} \frac{1}{\Omega} \frac{1}{r\Delta\phi}, \quad (16)$$

for the model with a weak magnetic field ( $\beta = 1000$ ). Fig. 3 shows the radial profile of  $Q_\phi$  (temporally and spatially  $\{\theta, \phi\}$  averaged). The fact that  $Q_\phi > 8$  indicates that the MRI is well resolved.

Because turbulence causes fluid elements in the vicinity of the planetary embryo (and more generally in the disk) to follow different trajectories in different realizations, a direct subtraction between simulations with  $L = L_c$  and  $L = 0$  does not provide useful information. We therefore consider the density maps without subtracting the cold case. As shown in Fig. 4, independently of the magnetic field strength, turbulent fluctuations generate cells of high and low density (i.e. strong density gradients) in the same area that would otherwise be occupied by hot lobes (see Fig. 1). Turbulence thus effectively wipes out the thermal lobes.

#### 3.2. Turbulence suppresses heating torques

The activation time of thermal torques is about one orbital period of the planetary embryo (Chametla & Masset 2021), whereas, as discussed above, the onset of MRI-driven turbulence occurs after about 2 orbital periods. In line with this, Fig. 5 shows that, for times  $t \leq 1.5$  orbits, the total torque  $\Gamma$  follows the behavior expected for the thermal torque in a laminar gas disk. During this phase, the torque is negative for  $L = 0$ , as expected for a non-luminous planetary embryo, whereas it becomes positive when

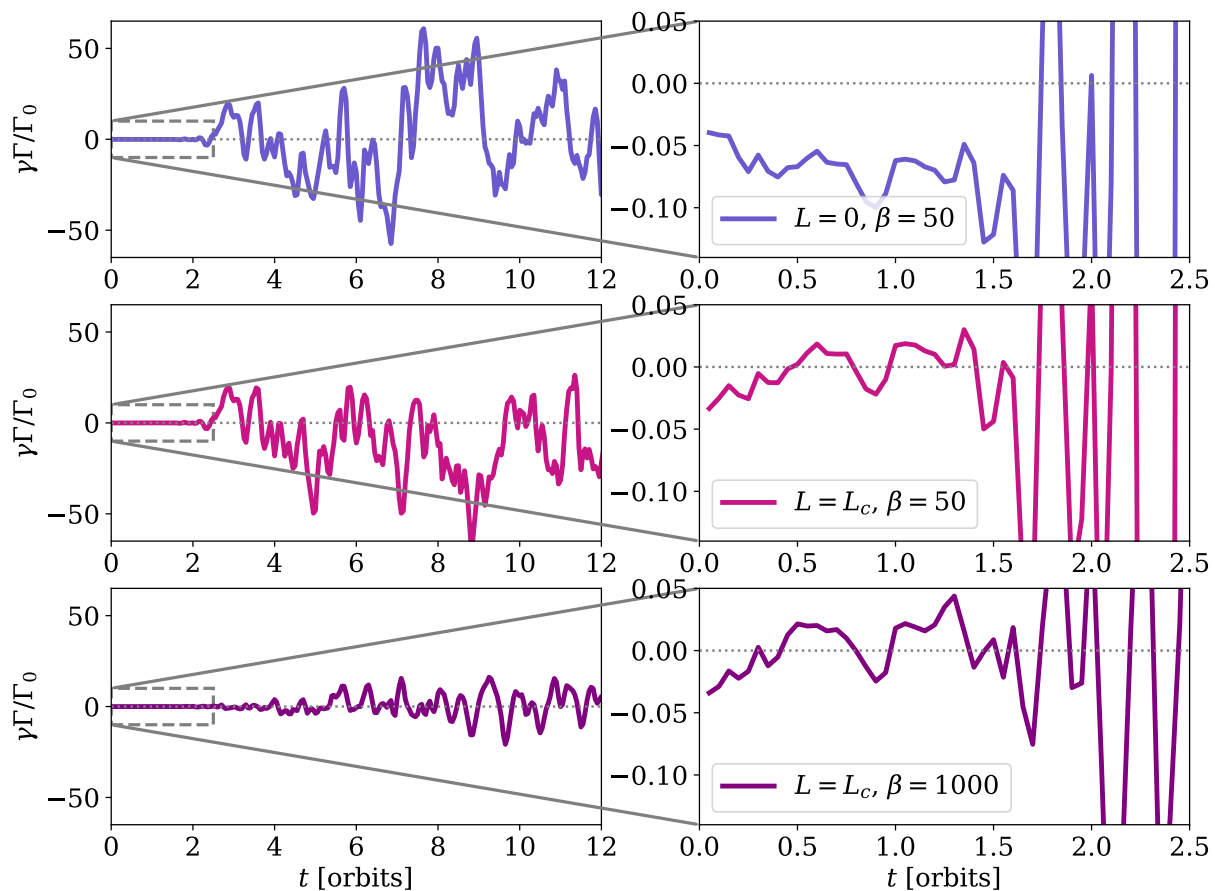


Fig. 5: Temporal evolution of the total torque  $\Gamma$  (in units of  $\Gamma_0/\gamma$ ) on the planetary embryo.

$L = L_c^2$ . Importantly, the torque behavior is largely insensitive to the value of  $\beta$  over this time interval (see the zoomed region in the right column of Fig. 5), reflecting the fact that turbulence has not yet developed in the disk.

For  $t > 1.5$  orbits, the situation changes drastically: the torque increases substantially in all cases and exhibits a strongly oscillatory behavior, reflecting the onset of the turbulence in the disk. A careful comparison of the torque in the cases where  $\beta = 50$  and  $L = 0$  and  $L = L_c$  (see first and second rows in Fig. 5) suggests that the torque falls into the stochastic regime (Nelson & Papaloizou 2004; Nelson 2005; Baruteau & Lin 2010; Comins et al. 2016). In the case  $L = L_c$ , the torque is shifted to higher (more positive) values, while the overall shape of  $\Gamma(t)$  remains largely unchanged, even up to  $\sim 3$  orbits. Furthermore, when the value of  $L$  is held fixed and  $\beta$  is increased from 50 to 1000, the amplitude of the torque oscillations is reduced (see the bottom row of Fig. 5). This indicates that the strength of the magnetic field governs the stochastic nature of the torque acting on the planetary embryo.

<sup>2</sup> Luminosities above the critical luminosity produce smaller changes in the total torque (i.e. they display an offset nearly constant in time between them, see Fig. 5 in Chametla & Masset (2021)) than the strong oscillations reported here when the MRI is active.

We expect the stochastic nature of the torque to be largely insensitive if the luminosity or mass of the planetary embryo are increased, since thermal torques become significantly cut off once the inequality  $(\lambda_c/H)M_{\text{th}} < M_p < M_{\text{th}}$  is satisfied, where  $M_{\text{th}} = c_s^3/G\Omega_p$  is the thermal mass (Velasco Romero & Masset 2020; Chametla & Masset 2021).

### 3.3. No traces of active magnetic resonances

When the toroidal magnetic field is sufficiently strong ( $\beta \lesssim 4$ ), the flow remains in a laminar regime, and magnetic resonances can make a significant contribution to the total torque. These resonances occur where the Doppler-shifted perturbation frequency in the fluid frame matches that of a slow MHD wave propagating along the magnetic field lines (Terquem 2003). The relative distance of these magnetic resonances from the planetary embryo is determined by the strength of the toroidal magnetic field through the  $\beta$ -parameter (Terquem 2003; Uribe et al. 2015):

$$|r_M - r_p| = \frac{2H_p}{3\sqrt{1+\beta_p}}, \quad (17)$$

where the subscript  $p$  indicates that the corresponding quantity should be evaluated at the position of the planetary embryo. As expected, when the magnetic field is very weak  $\beta_p \rightarrow \infty$ , the

position of the magnetic resonances converges to the position of the planetary embryo. These resonances can dominate the Lindblad torques, as they are located closer to the embryo than the Lindblad resonances.

To assess whether magnetic resonances operate within the thermal lobes prior to the onset of turbulence, we compare the radial separation  $|r_M - r_p|$  with the characteristic cutoff scale  $\lambda_c$ . In our models,  $|r_M - r_p| = 4.7 \times 10^{-3} r_p$  and  $|r_M - r_p| = 1.05 \times 10^{-3} r_p$ , for  $\beta = 50$  and  $\beta = 1000$ , respectively. On the other hand,  $\lambda_c = 2.2 \times 10^{-3}$  (from Eq. 12). Thus,  $\lambda_c$  and  $|r_M - r_p|$  are comparable. In our models, however, we find no evidence that magnetic resonances are active in the vicinity of the planetary embryo. Note that the timescale for the development of large-scale density waves associated with magnetic resonances is of the order of a few orbital periods (Uribe et al. 2015). Consequently, additional perturbations beyond those produced by the thermal lobes may not appear within the single orbital period shown in Fig. 1.

In the case of a relatively weak magnetic field ( $\beta \gg 1$ ), as in the models considered in this work, we have seen that the disk becomes turbulent. In principle, turbulence can suppress the heating torques, whereas the magnetic torques may persist at least partially. Returning to Fig. 4, we find no evidence of MHD ring-like waves such as those reported by Fromang et al. (2005, see their figure 3). We emphasize that the resolution used in our simulations is sufficient to resolve the characteristic density perturbation  $\lambda_c$  induced by planetary heating with at least ten grid cells, and therefore is also adequate to resolve the radial separation  $|r_M - r_p|$ . This indicates that the absence of slow MHD waves is not a resolution effect, but rather a consequence of the turbulent state of the disk, in which the magnetic field fluctuates locally on timescales shorter than those required for slow MHD waves to develop (see also Terquem 2003; Comins et al. 2016). This result complements what was previously reported for an isothermal disk with a toroidal magnetic field, in which magnetic resonances were likewise found to be ineffective (Uribe et al. 2015).

### 3.4. Thermal torques for Earth-mass planetary cores

In the previous subsections, we focused on the survival of thermal torques for planetary embryos with masses close to that of Mars in a turbulent disk. Since thermal torques reach their maximum efficiency for planetary cores of order one Earth mass (Velasco Romero & Masset 2020), we ran two additional models with  $M_p = 1 M_\oplus$  to assess whether thermal torques can survive in this mass range. Fig. 6 shows the resulting torques for  $L = L_c$  and two values of  $\beta$  (50 and 1000)<sup>3</sup>. As in the case of the planetary embryo, after 1.5 orbits turbulence induces strongly oscillatory torques for both values of  $\beta$ . We do not show maps of the gas density as they are very similar to those presented in Figure 4.

Large torque fluctuations, very similar to those shown in Figure 6, have also been observed in simulations of super-Earth planets ( $M_p > 3 M_\oplus$ ). In that case, they arise from vortices forming at the edge of the horseshoe region (Chametla & Masset 2021), as the gas dynamics become highly nonlinear with the Hill sphere for such planetary masses. Therefore, in regions where MRI turbulence develops, migration is expected to be

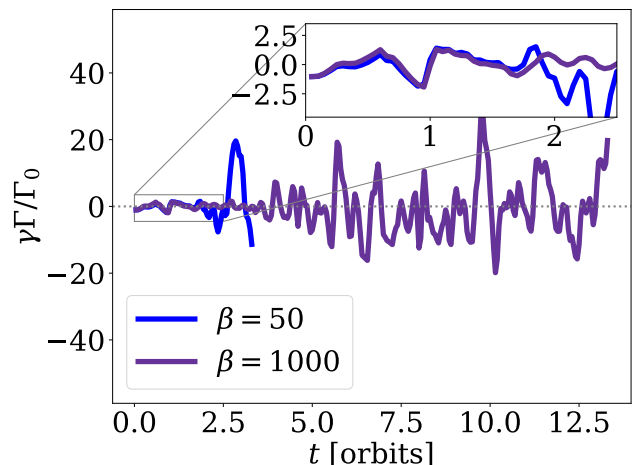


Fig. 6: Temporal evolution of the total torque  $\Gamma$  (in units of  $\Gamma_0/\gamma$ ) on a planet of mass  $M_p = 1 M_\oplus$ , for  $\beta = 50$  (blue lines) and  $\beta = 1000$  (purple lines).

stochastic for  $0.03 M_\oplus \lesssim M_p \lesssim 1 M_\oplus$  as a result of MRI turbulence and for  $M_p \gtrsim 3 M_\oplus$  owing to vortices.

Finally, we stress that the turn-off effect on the torque reported here is distinct from the cut-off effect investigated in Velasco Romero & Masset (2020).

## 4. Towards more complex models

In our simulations, we adopted a constant thermal diffusivity  $\chi = 10^{-5} r_p^2 \Omega_p$ . This value was chosen to allow the formation of hot thermal lobes around the luminous planet, enabling us to quantify the heating torques and construct a thermally controlled environment prior to the onset of MRI. In real protoplanetary disks, however,  $\chi$  is expected to vary spatially as it depends on local physical conditions, notably the gas density, temperature, and the opacity of the medium (Jiménez & Masset 2017, and references therein). These quantities are, in turn, influenced by the local dust concentration and by dust properties such as the grain size distribution and composition (Chametla et al. 2025). Therefore, more sophisticated models that include non-constant thermal diffusivity and an explicit treatment of dust are warranted and will be explored in future work.

## 5. Conclusions

In this study, we report the results of high-resolution 3D MHD simulations of a planetary embryo with a mass one third that of the planet Mars and for an Earth-mass core, embedded in a stratified gaseous disk with thermal diffusivity and a toroidal magnetic field. Our aim was to assess whether thermal torques can drive planetary migration in turbulent regions of a protoplanetary disk, such as the inner and outer regions of the disk located outside the so-called dead zone. To this end, we have considered two different luminosities for both the planetary embryo and core:  $L = 0$  corresponding to a cold thermal torque, and  $L = L_c$ , corresponding to a heating torque. In all cases, we find that, as turbulence develops in the disk, the thermal lobes are disrupted for both  $\beta = 50$  and  $\beta = 1000$ . In this turbulent regime, the total torque acting on the Mars planetary embryo and Earth-sized core

<sup>3</sup> The  $\beta = 50$  model evolved somewhat more slowly; due to the high computational cost, it was only integrated up to  $t = 3.3$  orbits, the limit imposed by cluster's walltime. Nevertheless, this duration was sufficient to capture the abrupt change in torque resulting from the onset of MRI.

displays the characteristic pattern of a stochastic torque, implying that its migration should proceed in the stochastic migration regime, similar to that observed in Nelson & Papaloizou (2004) and Comins et al. (2016). Given the results of Chametla & Masset (2021), which show that larger planetary masses also experience stochastic torques, we conclude that planets with masses  $0.03M_{\oplus} \lesssim M_p \lesssim 1M_{\oplus}$  and  $M_p \gtrsim 3M_{\oplus}$  are insensitive to thermal torques in a disk where turbulence is driven by MRI or vortices. Lastly, in agreement with the results of Comins et al. (2016), we found that the level of turbulence attained for  $\beta \geq 50$  renders magnetic resonances ineffective.

*Acknowledgements.* We thank the referee for the careful reading of the manuscript and for the constructive comments that helped improve the paper. The work of R.O.C. was supported by the Czech Science Foundation (grant 25-16507S). Computational resources were available thanks to the Ministry of Education, Youth and Sports of the Czech Republic through the e-INFRA CZ (ID:90254). Also, R.O.C. thanks Neal J. Turner for the fruitful discussions on this manuscript.

## References

- Balbus, S. A. & Hawley, J. F. 1991, *ApJ*, 376, 214  
 Baruteau, C. & Lin, D. N. C. 2010, *ApJ*, 709, 759  
 Baumann, T. & Bitsch, B. 2020, *A&A*, 637, A11  
 Bell, K. R. & Lin, D. N. C. 1994, *ApJ*, 427, 987  
 Benítez-Llambay, P., Krapp, L., & Pessah, M. E. 2019, *ApJS*, 241, 25  
 Benítez-Llambay, P., Masset, F., Koenigsberger, G., & Szulágyi, J. 2015, *Nature*, 520, 63  
 Benítez-Llambay, P. & Masset, F. S. 2016, *ApJS*, 223, 11  
 Chametla, R. O., Chrenko, O., Sánchez-Salcedo, F. J., et al. 2025, *A&A*, 704, A207  
 Chametla, R. O. & Masset, F. S. 2021, *MNRAS*, 501, 24  
 Chrenko, O. & Chametla, R. O. 2023, *MNRAS*, 524, 2705  
 Comins, M. L., Romanova, M. M., Koldoba, A. V., et al. 2016, *MNRAS*, 459, 3482  
 Cornejo, S., Masset, F. S., & Sánchez-Salcedo, F. J. 2023, *MNRAS*, 523, 936  
 Flock, M., Fromang, S., Turner, N. J., & Benisty, M. 2017, *ApJ*, 835, 230  
 Fromang, S., Terquem, C., & Nelson, R. P. 2005, *MNRAS*, 363, 943  
 Guilera, O. M., Cuello, N., Montesinos, M., et al. 2019, *MNRAS*, 486, 5690  
 Guilera, O. M., Miller Bertolami, M. M., Masset, F., et al. 2021, *MNRAS*, 507, 3638  
 Jiménez, M. A. & Masset, F. S. 2017, *MNRAS*, 471, 4917  
 Lega, E., Crida, A., Bitsch, B., & Morbidelli, A. 2014, *MNRAS*, 440, 683  
 Lyra, W. & Umurhan, O. M. 2019, *PASP*, 131, 072001  
 Masset, F. 2000, *A&AS*, 141, 165  
 Masset, F. S. 2017, *MNRAS*, 472, 4204  
 Nelson, R. P. 2005, *A&A*, 443, 1067  
 Nelson, R. P. & Papaloizou, J. C. B. 2004, *MNRAS*, 350, 849  
 Paardekooper, S., Dong, R., Duffell, P., et al. 2023, in *Astronomical Society of the Pacific Conference Series*, Vol. 534, *Protostars and Planets VII*, ed. S. Inutsuka, Y. Aikawa, T. Muto, K. Tomida, & M. Tamura, 685  
 Pierens, A. & Raymond, S. N. 2024, *A&A*, 684, A199  
 Sorathia, K. A., Reynolds, C. S., Stone, J. M., & Beckwith, K. 2012, *ApJ*, 749, 189  
 Terquem, C. E. J. M. L. J. 2003, *MNRAS*, 341, 1157  
 Uribe, A., Bans, A., & Königl, A. 2015, *ApJ*, 802, 54  
 Velasco Romero, D. A. & Masset, F. S. 2020, *MNRAS*, 495, 2063  
 Velasco-Romero, D. A., Masset, F. S., Morbidelli, A., et al. 2024a, *MNRAS*, 533, 807  
 Velasco-Romero, D. A., Masset, F. S., Morbidelli, A., et al. 2024b, *MNRAS*, 533, 807